

Virtual Inertia Scheduling (VIS) for Real-Time Economic Dispatch of IBR-Penetrated Power Systems

Buxin She ^{1b}, Graduate Student Member, IEEE, Fangxing Li ^{1b}, Fellow, IEEE, Hantao Cui ^{1b}, Senior Member, IEEE, Jinning Wang ^{1b}, Graduate Student Member, IEEE, Qiwei Zhang ^{1b}, Member, IEEE, and Rui Bo ^{1b}, Senior Member, IEEE

Abstract—A new concept called virtual inertia scheduling (VIS) is proposed to efficiently handle the increasing penetration of inverter-based resources (IBRs) in power systems. VIS is an inertia management framework that targets security-constrained and economy-oriented inertia scheduling and generation dispatch with a large scale of renewable generations. Specifically, it determines the appropriate power setpoint and reserved capacity of synchronous generators and IBRs, as well as the control modes and control parameters of IBRs to provide secure and cost-effective inertia support. First, a uniform system model is employed to quantify the frequency dynamics of IBR-penetrated power systems after disturbances. Leveraging this model, the s -domain and time-domain analytical responses of IBRs with inertia support capability are derived. Then, VIS-based real-time economic dispatch (VIS-RTED) is formulated to minimize generation and reserve costs, with full consideration of dynamic frequency constraints and the derived inertia support reserve constraints. The virtual inertia and damping of IBRs are formulated as decision variables. A deep learning-assisted linearization approach is further employed to address the non-linearity of dynamic constraints. Finally, VIS-RTED is demonstrated on a two-machine system and a modified IEEE 39-bus system. A full-order time-domain simulation is performed to verify the scheduling results.

Index Terms—Virtual inertia scheduling (VIS), real-time economic dispatch (RTED), inverter-based resource (IBR), virtual synchronous generator (VSG), frequency regulation.

NOMENCLATURE

Abbreviation

AGC Automatic generation control.

Manuscript received 19 February 2023; revised 20 May 2023 and 7 August 2023; accepted 12 September 2023. Date of publication 26 September 2023; date of current version 22 March 2024. This work was supported by the US DOD ESTCP Program under Grant EW20-5331 to complete this research work. Paper no. TSTE-00206-2023. (Corresponding author: Fangxing Li.)

Buxin She, Fangxing Li, Jinning Wang, and Qiwei Zhang are with the Department of Electrical Engineering and Computer Science, University of Tennessee, Knoxville, TN 37996 USA (e-mail: bshe@vols.utk.edu; fli6@utk.edu; jwang175@vols.utk.edu; qzhang41@vols.utk.edu).

Hantao Cui is with the School of Electrical and Computer Engineering, Oklahoma State University, Stillwater, OK 74078 USA (e-mail: h.cui@okstate.edu).

Rui Bo is with the Missouri University of Science and Technology, Rolla, MO 65409 USA (e-mail: rui.bo@ieee.org).

Color versions of one or more figures in this article are available at <https://doi.org/10.1109/TSTE.2023.3319307>.

Digital Object Identifier 10.1109/TSTE.2023.3319307

IBRs	Inverter-based resources.
DNNs	Deep neural networks.
PV	Photovoltaic.
SGs	Synchronous generators.
UC	Unit commitment.
VIS	Virtual inertia scheduling.
VSGs	Virtual synchronous generators.
RTED	Real-time economic dispatch.
RoCoF	Rate of change of frequency.
<i>Parameters</i>	
a^{sg}, a^{ibr}	Quadratic cost of SGs and IBRs.
$a_{i,t}^{sg}, a_{i,t}^{ibr}$	Quadratic cost of SG i and IBR i at time t .
α_m	Binary vector for DNN linearization.
b^{sg}, b^{ibr}	Linear cost of SGs and IBRs.
$b_{i,t}^{sg}, b_{i,t}^{ibr}$	Linear cost of SG i and IBR i at time t .
b_r^{sg}, b_r^{ibr}	Linear reserve cost of SGs and IBRs.
$b_{r,i,t}^{sg}, b_{r,i,t}^{ibr}$	Linear reserve cost of SG i and IBR i at time t .
c^{sg}, c^{ibr}	Constant cost of SGs and IBRs.
$c_{i,t}^{sg}, c_{i,t}^{ibr}$	Constant cost of SG i and IBR i at time t .
$D_i^{\max,ibr}$	Maximum virtual damping of IBR i .
$D_i^{\min,ibr}$	Minimum virtual damping of IBR i .
f_0	Nominal frequency.
LU_l	Line limit of line l .
$M_i^{\max,ibr}$	Maximum virtual inertia of IBR i .
$M_i^{\min,ibr}$	Minimum virtual inertia of IBR i .
N, N_{sg}, N_{ibr}	Number of buses, SGs, and IBRs.
$P_i^{\max,sg}$	Up power limit of SG i .
$P_i^{\min,sg}$	Down power limit of SG i .
$P_{i,t}^{\max,ibr}$	Up power limit of IBR i at time t .
$P_{i,t}^{\min,ibr}$	Down power limit of IBR i at time t .
$P_{i,t}^{sg}$	Up power reserve of SG i at time t .
$P_{i,t}^{sg}$	Down power reserve of SG i at time t .
$R, R_{sg,i}$	Droop gain factor of unified system and SG i .
$RoCoF_{lim}$	RoCoF limit.
S_i^{sg}	Rated capacity of SG i .
S_i^{ibr}	Rated capacity of IBR i .
T, T_{sg}, T_{ibr}	Time constant of a unified system, SGs, and IBRs.

Δf_{lim}	Frequency deviation limit.
<i>Variables</i>	
\mathbf{b}_m	Bias vector of DNN layer m .
D, D_{sg}	Synthetic damping of the unified system and SGs.
$D_{sg,i}$	Damping of SG i .
$D_{ibr,i}$	Virtual damping of IBR i .
$D_{i,t}^{ibr}$	Virtual damping of IBR i at time t .
\dot{f}_{max}	Maximum rate of change of frequency.
F, F_{sg}	The fraction of total power generated by the turbines of a unified system and SGs.
GSF	Generation shift factors.
$\bar{\mathbf{h}}, \mathbf{h}$	Up and down linearization limit of DNN layer.
K, K_{sg}	Mechanical power gain factor of a unified system and SGs.
L	Load.
$L_{i,t}$	Load i at time t .
M, M_{sg}	Synthetic inertia of the unified system and SGs.
$M_{sg,i}$	Inertia of SG i .
$M_{ibr,i}$	Virtual inertia of IBR i .
$M_{i,t}^{ibr}$	Virtual inertia of IBR i at time t .
P^{sg}, P^{ibr}	Power output of SGs and IBRs.
$P_{i,t}^{sg}, P_{i,t}^{ibr}$	Power output of SG i and IBR i at time t .
$P_{i,r,t}^{ibr}$	Power reserve of IBR i at time t .
s	Laplace operator.
t	Time.
t'_m	Time of IBR to output peak power.
w_d	Damping frequency of a unified system.
w_n	Nature frequency of a unified system.
\mathbf{W}_m	Linear coefficient vector of DNN layer m .
$\hat{\mathbf{z}}_m$	Linear output of DNN layer m .
\mathbf{z}_m	Activation function output of DNN layer m .
Δf_{nadir}	Frequency deviation nadir.
ΔP_e	Mismatch between mechanical power and electromagnetic power.
$\Delta P_{e,t}$	Mismatch between mechanical power and electromagnetic power at time t .
ΔP_{peak}	Peak power deviation of IBR.
$\Delta P_{i,\text{peak},t}$	Peak power deviation of IBR i at time t .
η	Inertial variable of uniform system frequency deviation.
α, β, η'	Internal variables of IBR power deviation.
ζ, ζ'	Damping ratio of a unified system and IBR power.
ϕ, ϕ'	Damping angle of a unified system and IBR power.
<i>Functions</i>	
$G(s)$	Closed-loop transfer function of a uniform frequency dynamics model.
$\Delta f(s)$	Transfer function of frequency deviation.
$\Delta P_e(s)$	Transfer function of electromagnetic power deviation.
$\Delta P_{ibr}(s)$	Transfer function of IBR power deviation.
$\Delta P(t)$	Time-domain function of IBR power deviation.

I. INTRODUCTION

A. Background

THE bulk power grid is transforming from a system dominated by synchronous generators (SGs) to one of hybrid SGs and inverter-based resources (IBRs). It is possible that the bulk power grid may become 100% IBR-based in the future [1], [2]. The transformation poses both opportunities and challenges to power systems [3]. On the one hand, IBRs make the best use of renewable energies, such as solar photovoltaics (PV), wind, tidal energy, and biomass energy, which are more environmentally friendly [4], [5], [6]. On the other hand, the integration of IBRs brings more uncertainty to the power grid and makes it difficult to predict and cooperate with the existing grid devices [7], [8]. IBRs have lower physical inertia than conventional SGs and thus pose a threat to maintaining system frequency stability [9], [10]. Hence, this paper focuses on the development of an urgently needed inertia management framework for IBR-penetrated power systems.

B. Literature Review

The literature that addresses low inertia issues can be roughly divided into two categories: i) methods that pursue inertia support from IBRs by designing new control strategies with inertia support capability; and ii) approaches that make better use of the inertia support capability of existing devices by integrating dynamic frequency constraints into an economic operation framework.

1) *IBR Control Algorithm With Inertia Support Capability*: Although IBRs have no rotating rotor mass, they can provide inertia support to the power system through elaborate control algorithm design. The concept of synchronverters, or virtual synchronous generators (VSGs), is proposed to provide ancillary services of synthetic inertia support for electric power systems [11], [12]. The grid-following IBRs track the frequency of the main grid and generate power reference using a proportional-differential controller, while the grid-forming IBRs measure the power out and generate frequency reference to avoid calculating differential terms that are sensitive to high frequency harmonics [13]. Fundamentally, VSG-controlled IBRs can provide virtual inertia support by rapidly increasing the active power injection right after a disturbance under the guidance of pre-configured control strategies.

Apart from the basic VSG control method, some improved algorithms have been proposed to enhance the inertia support capability of VSG-controlled IBRs. For example, a L_2 and L_{inf} norm controller was designed in [14] for VSG-controlled inverters, which improved IBRs' dynamic frequency response without increasing steady-state control effort. A linear-quadratic regulator based VSG was proposed in [15] for power systems with high inverter penetration, with the aim of making a tradeoff between the dynamic frequency constraints and the required control effort. In [16], an adaptive online virtual inertia and damping updating approach for virtual power plants were proposed to provide better inertia support for the main grid. In [17],

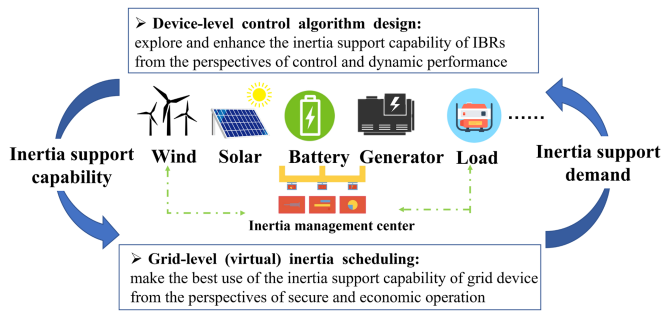


Fig. 1. Diagram of virtual inertia scheduling for future low inertia power systems.

a coordinated strategy for virtual inertial control and frequency damping control was proposed to explore the impact of virtual inertia and damping constant on frequency quality. An energy storage system with sufficient frequency reserves calculated by the final value theorem was configured in [18] to provide inertia support for the main grid. In [19], a control strategy was proposed for the H-bridge converter with a combination of maximum power point tracking and VSGs. The selected reserved cells set aside a certain amount of the total PV power to act as a power buffer between the VSG and PV power, which helped keep the grid frequency stable.

Excluding VSGs, it has been determined that droop-controlled IBRs may have limited inertia support capability due to modules in the control loop, i.e., phase lock loop (PLL), low-pass filter, and so on [20]. In summary, the existing IBR controllers are usually designed to relieve the problem of low inertia on the time scale of seconds and are not involved in the grid-level economic operation.

2) *Frequency-Constrained Economic Operation:* The conventional economic operation framework has three parts [21]: *i)* Unit commitment (UC) runs day-ahead scheduling to determine the unit's ON/OFF status; *ii)* Real-time economic dispatch (RTED) runs every 5 minutes to allocate the forecasted load among the committed units and schedule the reserve capacities; *iii)* Automatic generation control (AGC) is executed every 2-6 s to mitigate the frequency deviation and reduce tie-line flow error. Then, security frequency constraints are integrated into the above framework to address the low inertia problem, considering the inertia support capability of grid devices. This contributes to the development of security-constrained UC, security-constrained RTED, and security-constrained AGC as follows.

i) Security-constrained UC: A frequency-constrained UC strategy that takes wind farm support into account was proposed in [22], using the uniform system frequency model [23] and piece-wise linearization. In [24], a stochastic UC strategy was developed for low-inertia grids, where the nonlinear dynamic constraints of RoCoF and frequency nadir were transformed to bounded synthetic system parameters. In [25], a frequency reserve strategy was proposed for power systems under severe contingencies.

ii) Security-constrained RTED: Frequency constraints were considered in [26]. A confidence interval-based and distributionally robust RTED was proposed to strike a balance between

security and economy. The operational risk was estimated based on wind power curtailment and load shedding resulting from wind power disturbance. Considering the secondary frequency regulation cost, a data-driven, and distributionally robust optimization was developed in [27] for RTED.

iii) Security-constrained AGC: An AGC-constrained economic dispatch was formulated in [21] with a full consideration of the short-term and long-term forecast. The adaptive and coordinated AGC strategy updated the regulation reserve online while guaranteeing the AGC variation constraints.

In general, the dynamic frequency response and the inertia support from IBRs are gaining more and more attention in the economic operation of power systems.

C. Motivation and Concept of Virtual Inertia Scheduling

1) *Motivation:* Following traditional practices, the device-level control algorithm design of IBRs and system-level economic operation has always been decoupled due to their distinct operational timescales. The former focuses on the dynamic control of power electronics to have the desired inertia support capability, while the latter usually works on demand-supply balance and cost-saving, assuming the preconfigured dynamic characteristics of the system devices. This is solid for conventional SG-dominated power systems because the response speed of SGs is relatively slow, and their parameters are usually fixed once configured. For example, the typical response time constant of the prime mover of a SG is 2 s and the start-up and shut-down time of a gas SG is 30 mins. SGs' inertia constants and starting/closing time are determined by their physical configuration. However, the high penetration of IBRs challenges this assumption because IBRs have much faster electromagnetic responses than SGs and their control parameters can be changed adaptively in seconds or even milliseconds.

Although the high penetration of IBRs brings low inertia and quick dynamic features to power systems, it also opens the possibility of a more advanced scheduling framework by leveraging IBRs' controllability and flexibility. In the existing frequency-constrained scheduling framework, IBRs are generally considered passive devices with constant control parameters. Motivated by better cooperation of device-level IBR control and grid-level economic operation, this article proposes the concept of virtual inertia scheduling (VIS) for future low inertia power systems.

2) *Concept of VIS:* VIS is an inertia management framework that targets security-constrained and economy-oriented inertia scheduling and power dispatch of power systems with a large scale of renewable generation. As shown in Fig. 1, the device-level control algorithm design explores the inertia support capability of IBRs and provides scheduling options (operation mode and operation parameters) for VIS. Then, VIS is set up at the grid level to make the best use of the inertia support capability of IBRs. Compared with the conventional economic operation framework, VIS further addresses low inertia issues by leveraging the controllability and flexibility of power electronics-based devices that can respond quickly to scheduling results. It not only schedules the power setting points of system devices, but also

determines the real-time operation modes and real-time control parameters of IBRs, as well as the required power reserve for inertia support.

3) *Feasibility of VIS*: From a technical standpoint, changing the inertia or damping parameters of IBRs within minutes or even shorter is feasible. Some research has focused on the online tuning of virtual inertia and damping, with most efforts concentrated on the time scale of seconds [28], [29], [30], [31]. For instance, an online adaptive VSG control strategy was proposed in [29], which considered both weak and strong power system conditions and tuned virtual inertia and damping based on online grid impedance estimation results. Similarly, [31] proposed an adaptive VSG strategy for multi-terminal DC systems that adaptively adjusted the control parameters depending on the frequency margin of every AC network. Furthermore, IBRs are expected to participate in the power system ancillary service market in the future. Currently, virtual inertia support is not included in the ancillary service market. However, considering the increasing penetration of IBRs, it becomes imperative to provide inertia support services to ensure the secure operation of low-inertia power systems.

Once the ancillary service market is established, the independent system operators may calculate the necessary virtual inertia, allowing IBR owners to adjust inertia or damping parameters accordingly based on the bidding results. To facilitate the development of the inertia market, several challenges need to be addressed. First, from a market design perspective, appropriate market rules should be formulated to fairly allocate benefits to participants and incentivize inertia support. Second, from a technical perspective, it is crucial to establish well-defined inertia support requirements (responsibility). Furthermore, ensuring dynamic performance and stability guarantee is paramount, given that parameter configurations can significantly impact the dynamics of IBRs and the overall system. This article included small-signal stability checks in the workflow, and further performed time-domain simulation to verify the system stability based on the VIS results.

In general, VIS addresses the needs of future power grids and represents pioneering work in integrating inertia service into the system-level economic operation. It can fuse with each level of the economic operation framework, including UC, RTED, and AGC. To narrow down the research topic, this article focuses on VIS-based real-time economic dispatch (VIS-RTED) for power systems with high penetration of IBRs. Specifically, this article focuses on a VIS-RTED that runs every 5 minutes to schedule the power setting points and reserve capacities of both SGs and IBRs, as well as the virtual inertia and damping of IBRs, to provide secure and cost-effective inertia support.

D. Contribution and Organization

Four contributions of this manuscript are summarized as follows:

- Proposes the concept of VIS, an inertia management framework that targets the security-constrained and economy-oriented inertia scheduling and power dispatch of IBR-penetrated power systems.

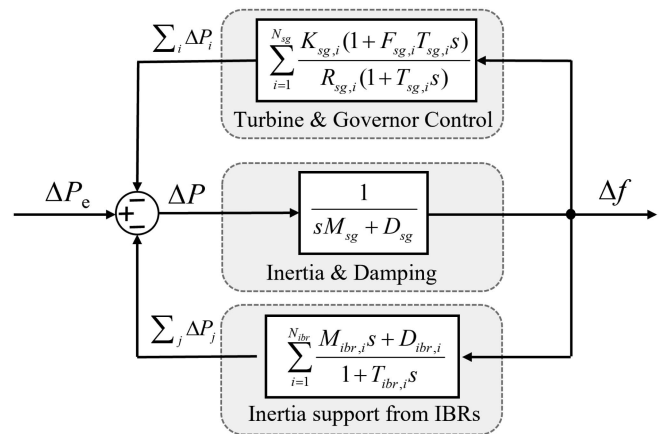


Fig. 2. Uniform frequency dynamics model of IBR-penetrated power system [15].

- Derives the time-domain analytical response of IBRs with inertia support capability after disturbances, especially the analytical expressions of the power response, the peak power, and the time to reach the peak power.
- Formulates VIS-RTED for IBRs-penetrated low inertia power systems and linearizes it using deep neural networks (DNNs). The derived peak power is added as a power reserve constraint of IBRs, and the virtual inertia and damping are formulated as decision variables of the optimization problem.
- Performs full-order time-domain simulation to validate the formulated VIS-RTED, rather than utilizing simplified transfer function models.

The rest of this article is organized as follows. Section II introduces the dynamic model of an IBR-penetrated power system, which is then integrated into the optimization formulation. The proposed VIS is integrated into RTED in Section III, followed by a deep learning assisted approach to linearize the dynamic constraints. Then, Section V conducts case studies and makes comparisons with the existing methods. Conclusions are drawn in Section VI.

II. DYNAMIC MODELING OF IBR-PENETRATED POWER SYSTEM

This section introduces the dynamic modeling of IBR-penetrated power systems, including the uniform frequency dynamics model and analytical frequency and power response. These frequency and power metrics serve as critical constraints within the VIS-RTED framework in Section III.

A. Uniform Frequency Dynamics Model

By referring to [15], this article employs a simplified, but sufficiently accurate, uniform frequency dynamics model of an IBR-penetrated power system. As shown in Fig. 2, the uniform model considers the dynamics of the turbine and governor of SGs and the inertia support from IBRs. It estimates the frequency response of low inertia power systems after a disturbance. The closed-loop transfer function of the uniform frequency dynamics

model is shown in (1).

$$G(s) = \frac{\Delta f(s)}{\Delta P_e(s)} = \underbrace{\left[(sM_{sg} + D_{sg}) + \sum_{i=1}^{N_{sg}} \frac{K_{sg_i} (1 + sF_{sg_i} T_{sg_i})}{R_{sg_i} (1 + sT_{sg_i})} \right]}_{\text{SGs}} + \underbrace{\left[\sum_{j=1}^{N_{ibr}} \frac{sM_{ibr_j} + D_{ibr_j}}{1 + sT_{ibr_j}} \right]}_{\text{IBRs}}^{-1} \quad (1)$$

Assume all SGs have equal time constants ($T_{sg} = T$), and the inverter time constants T_{ibr} are 2-3 orders of magnitude lower than T . Then, (1) is transformed as follows.

$$G(s) = \frac{\Delta f(s)}{\Delta P_e(s)} = \frac{1}{MT} \frac{1 + sT}{s^2 + 2\zeta w_n s + w_n^2} \quad (2)$$

where

$$\begin{cases} w_n = \sqrt{\frac{D+R}{MT}} \\ \zeta = \frac{M+T(D+F)}{2\sqrt{MT(D+R)}} \\ M = \frac{\sum_{i=1}^{N_{sg}} M_{sg,i} S_i^{sg} + \sum_{i=1}^{N_{ibr}} M_{ibr,i} S_i^{ibr}}{\sum_{i=1}^{N_{sg}} S_i^{sg} + \sum_{i=1}^{N_{ibr}} S_i^{ibr}} \\ D = \frac{\sum_{i=1}^{N_{sg}} D_{sg,i} S_i^{sg} + \sum_{i=1}^{N_{ibr}} D_{ibr,i} S_i^{ibr}}{\sum_{i=1}^{N_{sg}} S_i^{sg} + \sum_{i=1}^{N_{ibr}} S_i^{ibr}} \\ F = \frac{\sum_{i=1}^{N_{sg}} K_{sg,i} F_{sg,i} S_i^{sg} / R_{sg,i}}{\sum_{i=1}^{N_{sg}} S_i^{sg}} \\ R = \frac{\sum_{i=1}^{N_{sg}} K_{sg,i} S_i^{sg} / R_{sg,i}}{\sum_{i=1}^{N_{sg}} S_i^{sg}} \end{cases} \quad (3)$$

B. Analytical Frequency Response

Assume a stepwise disturbance in the electrical power. Then the analytical s -domain frequency response is derived in (4).

$$\Delta f(s) = \frac{\Delta P_e}{MT} \frac{1 + sT}{s(s^2 + 2\zeta w_n s + w_n^2)} \quad (4)$$

Perform an inverse Laplace transform in (4), then the analytical time-domain frequency response is derived as follows.

$$\Delta f(t) = \frac{\Delta P_e}{MTw_n^2} [1 - e^{-\zeta w_n t} \eta \sin(w_d t + \phi)] \quad (5)$$

where

$$\begin{cases} w_d = \sqrt{1 - \zeta^2} w_n \\ \eta = \sqrt{\frac{1 - 2T w_n \zeta + T^2 w_n^2}{1 - \zeta^2}} \\ \tan \phi = \frac{w_d}{-T w_n^2 + \zeta w_n} \end{cases} \quad (6)$$

The time instance of frequency nadir is determined by finding the instance at which the derivation of (5) is equal to 0. Then, the frequency nadir is derived by substituting the time instance into (5), and the maximum RoCoF occurs at $t = 0^+$.

$$\Delta f_{\text{nadir}} = \frac{\Delta P_e}{MTw_n^2} [1 - \sqrt{1 - \zeta^2} \eta e^{-\zeta w_n t_m}] \quad (7)$$

$$\dot{f}_{\text{max}} = \Delta \dot{f}(0^+) = -\frac{\Delta P_e}{M} \quad (8)$$

C. Analytical Power Response of IBRs

The s -domain power response is obtained by integrating the s -domain frequency response into the feedback loop of VSG-controlled IBRs.

$$\Delta P_{ibr}(s) = \frac{\Delta P_e (M_{ibr} s + D_{ibr}) (1 + sT)}{MT s (s^2 + 2\zeta w_n s + w_n^2)} \quad (9)$$

(9) is simplified as (10) by introducing some internal variables α and β .

$$\Delta P_{ibr}(s) = \frac{\Delta P_e D_{ibr}}{MT w_n^2} \left[-\frac{1}{s} + \frac{\alpha s + \beta}{s^2 + 2\zeta w_n s + w_n^2} \right] \quad (10)$$

where

$$\begin{cases} \alpha = 1 - \frac{M_{ibr} T w_n^2}{D_{ibr}} \\ \beta = -T w_n^2 + 2\zeta w_n - \frac{M_{ibr} w_n^2}{D_{ibr}} \end{cases} \quad (11)$$

Perform an inverse Laplace transform on (10) and combine the sine and cosine functions. Then, the time-domain power response is obtained as follows.

$$\Delta P(t) = \frac{\Delta P_e D_{ibr}}{MT w_n^2} [-1 + \alpha \eta' e^{-\zeta w_n t} \sin(w_d t + \phi')] \quad (12)$$

where

$$\begin{cases} \tan \phi' = \frac{w_d}{\beta/\alpha - \zeta w_n} \\ \eta' = \sqrt{1 + \left(\frac{\beta/\alpha - \zeta w_n}{w_d} \right)^2} \end{cases} \quad (13)$$

Similar to the derivation of the frequency nadir, the time instance t_m' of peak power is obtained by setting the derivative of (12) equal to 0. Substituting t_m' into (12) yields the peak power.

$$\Delta \dot{P}_{ref}(t_m') = 0 \quad (14)$$

$$t_m' = \frac{1}{w_d} \tan^{-1} \left[\frac{(\beta - 2\zeta \alpha w_n) w_d}{\zeta \beta w_n - \zeta^2 w_n^2 \alpha + \alpha w_d^2} \right] \quad (15)$$

$$\Delta P_{\text{peak}} = \frac{\Delta P_e D_{ibr}}{MT w_n^2} [-1 + \alpha \eta' \sqrt{1 - \zeta^2} e^{-\zeta w_n t_m'}] \quad (16)$$

D. Typical Power Curve of IBRs

This subsection plots typical power curves of IBRs with inertia support capability, highlighting the importance of active power reserve in frequency (inertia) provision.

Assume three IBRs are providing inertia support for a low inertia system, but assigned distinct virtual inertia values. Appendix A details the control parameters. Then, plug these parameters into the uniform frequency dynamics model and plot the system response. Fig. 3 shows the power and frequency response of IBRs following a step disturbance at 5 seconds. Based on Fig. 3, the observations are three-fold:

- Three IBRs work together for frequency provision by instantaneously increasing the active power injection to the main grid after the step disturbance. They have distinct power responses but same frequency responses for the whole system.
- The virtual inertia of IBR1 is set to zero ($M_{ibr,1} = 0$), and its output displays an inverted frequency trajectory with the same overall shape. They reach the peak or nadir

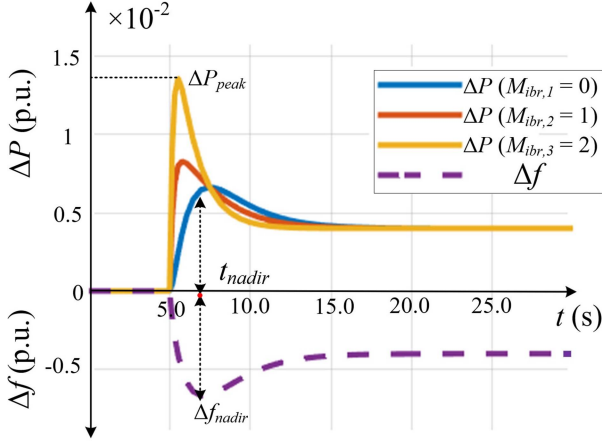


Fig. 3. Typical power and frequency responses of IBRs after step disturbance.

simultaneously since the calculation of ΔP_e is based on the product of frequency deviation and virtual damping.

- When assigned large virtual inertia, IBR2 and IBR3 exhibit more pronounced and rapid power responses to step disturbances. This results in higher peak power output and a shorter time to reach the peak.

SGs support the main grid by releasing the energy stored in the rotors, which is more of a mechanical process with physical support. In contrast, IBRs rely on fast power electronics discharge for inertia support, which allows for flexible and controllable support through sophisticated controller and parameter design. The inertia support energy of IBRs is typically stored in DC-side capacitors or battery energy storage systems, and is much lower than the mechanical energy stored in SG rotors. Insufficient power reserve for IBRs can result in DC-side voltage dips and even IBR trips [32]. Therefore, it is crucial to allocate inertia support reserves [19] or some headroom from the maximum power point [11] for online IBR inertia support, as detailed in VIS formulation in the following section.

III. FORMULATION OF VIRTUAL INERTIA SCHEDULING FOR REAL-TIME ECONOMIC DISPATCH

This section introduces the standard RTED and then formulates VIS-RTED. A deep learning assisted algorithm is used to linearize the dynamic constraints in VIS-RTED.

A. Conventional Real-Time Economic Dispatch

Given the predicted load profile, the conventional RTED is formulated as a multi-interval optimization problem with the objective of minimizing the total generation cost while also satisfying the network and generation constraints. Equations (17)–(24) show the standard formulation of RTED.

$$\min_P \sum_{t \in T} \underbrace{\left[\sum_{i=1}^{N_{sg}} \left(a_{i,t}^{sg} P_{i,t}^{sg2} + b_{i,t}^{sg} P_{i,t}^{sg} + c_{i,t}^{sg} + b_{r,i,t}^{sg} P_{i,t}^{sg} \right) \right]}_{SG}$$

$$+ \underbrace{\sum_{i=1}^{N_{ibr}} \left(a_{i,t}^{ibr} P_{i,t}^{ibr2} + b_{i,t}^{ibr} P_{i,t}^{ibr} + c_{i,t}^{ibr} \right)}_{IBR} \quad (17)$$

For $\forall t \in \{1, \dots, T\}$, s.t.,

$$\sum_{i=1}^{N_{sg}} P_{i,t}^{sg} + \sum_{i=1}^{N_{ibr}} P_{i,t}^{ibr} - \sum_{i=1}^{N_l} L_{i,t} = 0 \quad (18)$$

$$\sum_{i=1}^N GSF_{l,t} (P_{i,t}^{sg} + P_{i,t}^{ibr} - L_{i,t}) \leq LU_l \quad (19)$$

$$\sum_{i=1}^N GSF_{l,t} (P_{i,t}^{sg} + P_{i,t}^{ibr} - L_{i,t}) \geq -LU_l \quad (20)$$

$$P_{i,t}^{sg} + P_{i,r,u,t}^{sg} \leq P_i^{\max,sg} \quad (21)$$

$$P_{i,t}^{sg} - P_{i,r,d,t}^{sg} \geq P_i^{\min,sg} \quad (22)$$

$$P_{i,t}^{ibr} \leq P_{i,t}^{\max,ibr} \quad (23)$$

$$P_{i,t}^{ibr} \geq P_{i,t}^{\min,ibr} \quad (24)$$

where (18) is power balance constraint; (19)–(20) are the transmission line thermal constraints; (21)–(22) are SG generation constraints with regulation up or regulation down reserve; and (23)–(24) are IBR generation constraints.

B. VIS-Based Real-Time Economic Dispatch

1) *Mathematical Formulation:* The proposed VIS-RTED extends the standard RTED and includes critical modifications for low-inertia power systems with high penetration of IBRs. These modifications are as follows.

- The inclusion of frequency nadir and RoCoF constraints, which are essential for ensuring the security of IBRs-penetrated low-inertia power systems.
- Formulation of M_{ibr} and D_{ibr} as decision variables to optimize the frequency support from IBRs.
- The inclusion of up and down frequency reserve constraints for IBRs to prevent the risk of DC voltage dips and device trips.
- The incorporation of IBR reservation cost into the objective function, which serves as the opportunity cost for frequency prevision.

Then, VIS-RTED is formulated as follows.

$$\min_{P,M,D} \sum_{t \in T} \underbrace{\left[\sum_{i=1}^{N_{sg}} \left(a_{i,t}^{sg} (P_{i,t}^{sg})^2 + b_{i,t}^{sg} P_{i,t}^{sg} + c_{i,t}^{sg} + b_{r,i,t}^{sg} P_{i,t}^{sg} \right) \right]}_{SG} + \underbrace{\sum_{i=1}^{N_{ibr}} \left(a_{i,t}^{ibr} (P_{i,t}^{ibr})^2 + b_{i,t}^{ibr} P_{i,t}^{ibr} + c_{i,t}^{ibr} + b_{r,i,t}^{ibr} P_{i,t}^{ibr} \right)}_{IBR} \quad (25)$$

For $\forall t \in \{1, \dots, T\}$, s.t. Constraints (18)–(22),

$$P_{s,i,t}^{ibr} + P_{i,r,t}^{ibr} \leq P_{i,t}^{\max,ibr} \quad (26)$$

$$P_{i,t}^{ibr} - P_{i,r,t}^{ibr} \geq P_{i,t}^{\min,ibr} \quad (27)$$

$$P_{i,r,t}^{ibr} = \Delta P_{i,peak,t}^{ibr} \quad (28)$$

$$M_i^{\min,ibr} \leq M_{i,t}^{ibr} \leq M_i^{\max,ibr} \quad (29)$$

$$D_i^{\min,ibr} \leq D_{i,t}^{ibr} \leq D_i^{\max,ibr} \quad (30)$$

$$-\text{RoCoF}_{\text{lim}} \leq f_0 \frac{\Delta P_{e,t}}{M_t} \leq \text{RoCoF}_{\text{lim}} \quad (31)$$

$$-\Delta f_{\text{lim}} \leq \Delta f_{\text{nadir},t} \leq \Delta f_{\text{lim}} \quad (32)$$

$$\Delta P_{e,t} = \sum_{i=1}^{N_t} L_{i,t} - \sum_{i=1}^{N_t} L_{i,t-1} \quad (33)$$

where (26)–(28) integrate the analytical peak power ΔP_{peak} derived in (16) into IBR generation constraints (23)–(24); (29)–(30) are the virtual inertia and damping constraints of IBRs; (31) is RoCoF constraint integrating (8); (32) is frequency nadir constraint integrating (7); and (33) is the disturbance caused by load change, which can result in frequency deviation and can make (31)–(32) binding constraints.

2) *Connection Between Dynamics and Economy*: The proposed VIS-RTED addresses the low inertia issue of power systems with high penetration of IBRs by leveraging their controllability and flexibility and integrating dynamic constraints into conventional economic dispatch framework.

By assigning large values to M_{ibr} and D_{ibr} , IBRs can provide better inertia support and contribute to better dynamic frequency performance after disturbances, with a small frequency nadir and RoCoF. However, as shown in Fig. 3, larger virtual inertia results in larger peak power after disturbance, which requires more generation reserve from IBRs and thus increases generation cost. In particular, the marginal generation cost of IBRs is usually much lower than that of SGs, and less generation from IBRs will result in more generation from SGs and a much higher generation cost. Therefore, it is crucial to strike a balance between dynamic performance and generation cost by optimizing M_{ibr} and D_{ibr} . This highlights the contribution of the VIS-RTED in enabling such tradeoff, which is a major motivation of this research work.

In summary, the VIS-RTED enables security-constrained and economy-oriented inertia management and real-time power dispatch by integrating VIS with the existing frequency-regulated economic operation framework.

C. Deep Learning Assisted Linearization

Although Section III-B rigorously formulated VIS-RTED, it is difficult to directly solve it with commercial solvers because frequency nadir and inertia support reserves bring non-linear and non-convex constraints to VIS-RTED. Following the working in [33], [34], a deep learning assisted linearization approach is employed to linearize constraints (26)–(27) and (32).

Two training datasets are generated within the feasible region of functions (7) and (16), with which two DNNs can be trained to predict the frequency nadir and IBR peak power. By introducing some binary variables and two large enough constants, the trained neural networks with activation function ReLU are

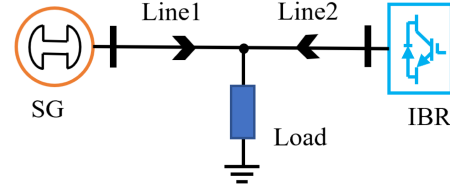


Fig. 4. Diagram of the two-machine system.

transformed into mix-integer linear functions. Equations (34) and (35) show the expressions of the m th hidden layer before and after linearization, respectively.

$$\begin{cases} \hat{z}_m = \mathbf{W}_m \mathbf{z}_{m-1} + \mathbf{b}_m \\ \mathbf{z}_m = \max(\hat{z}_m, \mathbf{0}) \end{cases} \quad (34)$$

$$\begin{cases} \mathbf{z}_m \leq \hat{z}_m - \underline{\mathbf{h}} \odot (\mathbf{1} - \mathbf{a}_m) \\ \mathbf{z}_m \geq \hat{z}_m \\ \mathbf{z}_m \leq \bar{\mathbf{h}} \odot \mathbf{a}_m \\ \mathbf{z}_m \geq \mathbf{0} \end{cases} \quad (35)$$

where \odot is bitwise multiplication; \mathbf{a}_m is a binary vector; and $[\underline{\mathbf{h}}, \bar{\mathbf{h}}]$ forms a vector interval that is large enough to contain all possible values of \mathbf{z}_m .

Then, the two linearized networks can replace ΔP_{peak}^{ibr} and Δf_{nadir} in (26)–(27) and (32). More transformation details can be found in [33] and [34]. Because the training datasets are generated based on the analytical expressions derived in Section II instead of case-by-case numerical simulations, the trained neural networks have a high generalization capability and can be easily applied to other power systems while still retaining high prediction accuracy.

IV. CASE STUDY

This section presents case studies to validate the proposed VIS-RTED on two test systems: a two-generator system and a modified IEEE 39-bus system. A full-order time-domain simulation is further conducted to verify the scheduling results.

A. Two-Machine System

This subsection uses a simple two-machine system in Fig. 4 to exemplify the formulation of VIS-RTED and highlights the importance of integrating the dynamic frequency and power response into economic dispatch.

1) *Single-Interval VIS-RTED Formulation*: The current load L is 2.0 p.u. and the rest parameters are shown in Table IV, Appendix B. Assume there is a predicted load increase in the next interval ($\Delta P_e = -0.05$ p.u.). Formulate single-interval VIS-RTED to determine the power setting points P_{sg} and P_{ibr} and control parameters M_{ibr} and D_{ibr} , with the objective of minimizing the generation cost while also satisfying the operational security constraints. Assume that the frequency nadir and RoCoF limits are 0.1 Hz and 0.5 Hz/s [35], respectively. After the predefined disturbance, frequency nadir and RoCoF should be within the expected range, and the peak power of IBR should not exceed its capacity. Then, single-interval VIS-RTED ($T = 1$) using deep-learning assisted linearization is formulated

as follows.

$$\min_{P_{sg}, P_{ibr}, M_{ibr}, D_{ibr}} a^{sg} (P^{sg})^2 + b^{sg} P^{sg} + c^{sg} + b_r^{sg} P_r^{sg} + a^{ibr} (P^{ibr})^2 + b^{ibr} P^{ibr} + c^{ibr} + b_r^{ibr} P_r^{ibr} \quad (36)$$

$$s.t. \quad P_{sg} + P_{ibr} - L = 0 \quad (37)$$

$$-LU_1 \leq P_{sg} \leq LU_1 \quad (38)$$

$$-LU_2 \leq P_{ibr} \leq LU_2 \quad (39)$$

$$P^{sg} + P_r^{sg} \leq P^{\max, sg} \quad (40)$$

$$P^{sg} - P_r^{sg} \geq P^{\min, sg} \quad (41)$$

$$P^{ibr} + \Delta P_{peak}^{ibr} \leq P^{\max, ibr} \quad (42)$$

$$P^{sg} - \Delta P_{peak}^{ibr} \geq P^{\min, ibr} \quad (43)$$

$$M^{\min, ibr} \leq M^{ibr} \leq M^{\max, ibr} \quad (44)$$

$$D^{\min, ibr} \leq D^{ibr} \leq D^{\max, ibr} \quad (45)$$

$$-\text{RoCoF}_{\text{lim}} \leq f_0 \frac{\Delta P_e}{M} \leq \text{RoCoF}_{\text{lim}} \quad (46)$$

$$-\Delta f_{\text{lim}} \leq \Delta f_{\text{nadir}, t} \leq \Delta f_{\text{lim}} \quad (47)$$

where ΔP_{peak}^{ibr} and Δf_{nadir} derived in (7) and (16) are linearized by two DNNs as follows.

$$\begin{cases} \Delta P_{peak}^{ibr} = \text{DNN}_1(\Delta P_e, M, D, R, F, T) \\ \Delta f_{\text{nadir}} = \text{DNN}_2(\Delta P_e, M, D, R, F, T) \end{cases} \quad (48)$$

2) *Deep Learning Training Results:* Two multilayer perceptions are configured to predict the frequency nadir and VSG peak power, each with 1 hidden layer and 64 neurons. For each DNN, a dataset with a sample size of 20,000 was generated for training in PyTorch. Fig. 5 shows the training results, where (a) and (b) use a logarithmic scaled horizontal axis. After training for 1,000 epochs, the two DNNs can accurately predict the frequency nadir and VSG peak power.

3) *Scheduling Results and Dynamic Response:* The mixed-integer linear optimization model shown in (36)–(48) is solved with the following values: $P_{sg} = 1.013$ p.u., $P_{ibr} = 0.987$ p.u., $M_{ibr} = 4$ p.u., $D_{ibr} = 1$ p.u., and $M = 6$ p.u., resulting in a minimized cost of \$11.54 for a single RTED interval.

Given that a load increase occurs at 5 s, the dynamic response of the two-machine system is plotted in Fig. 6 based on the uniform frequency dynamic model in Fig. 2. The red curves demonstrate how the formulated VIS optimally harnesses the inertia support capabilities of IBRs. Notably, the maximum RoCoF after the disturbance is precisely 0.5 Hz/s, and the IBR's output reaches its maximum capacity, successfully adhering to the dynamic security constraints. By setting $M_{ibr} = 6$, the IBR requires additional headroom to prevent the capacity violation, potentially incurring opportunity costs. Conversely, with $M_{ibr} = 0$, the synthetic inertia constant M is too small to prevent RoCoF violation immediately after the disturbance. These observations underscore the significance of balancing dynamic performance and economic considerations, as exemplified by the results presented.

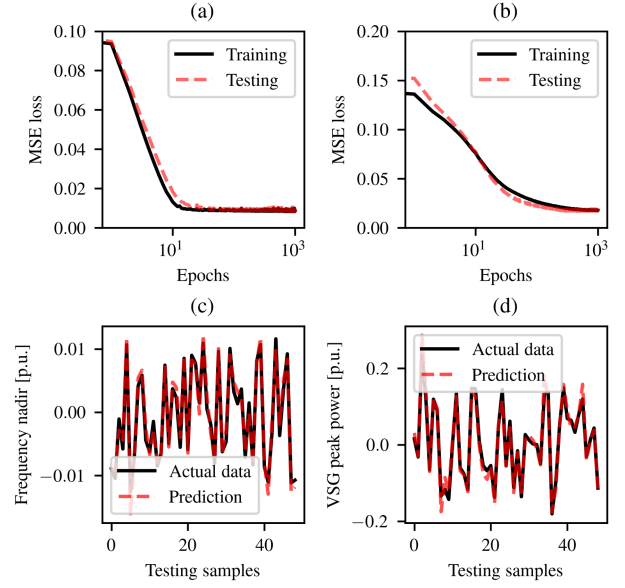


Fig. 5. DNN training results: (a) Training loss of frequency nadir prediction; (b) Training loss of IBR peak power prediction; (c) Testing of frequency nadir prediction; (d) Testing of IBR peak power prediction.

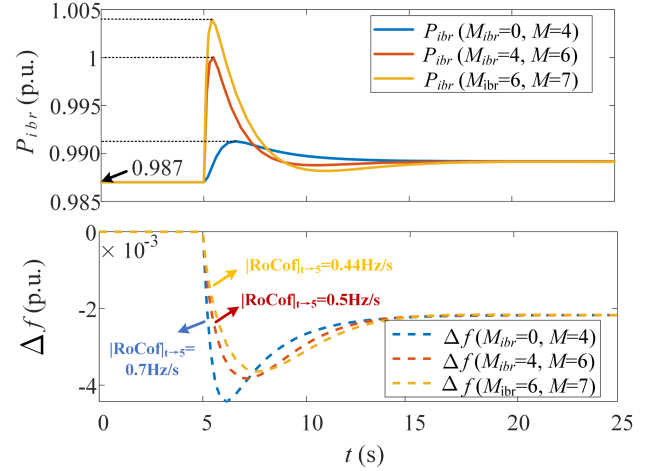


Fig. 6. Dynamic performance of the two-machine system with VIS-RTED scheduling results.

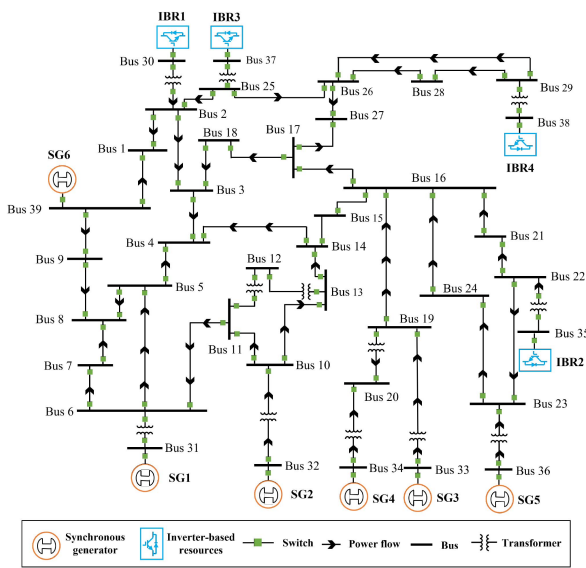
B. Overview of IEEE 39-Bus System

The proposed VIS-RTED is further demonstrated on a modified 39-bus system [36] with $S_{base} = 100$ MVA.

1) *Modified 39-Bus System:* Fig. 7(a) shows the geographical diagram of the original 39-bus system visualized in CURENT Large-scale Testbed (LTB)'s AGVis tool [37], [38], and Fig. 7(b) shows the one-line diagram of the modified system. Four SGs connected to Buses 30, 35, 37, and 38 are replaced by IBRs with capacities of 900 MW, 800 MW, 700 MW, and 1,000 MW, respectively. Assume the maximum M of an IBR is not larger than that of an SG with the same capacity, and the range of IBRs' virtual inertia and damping are at $[0, 8.0]$ p.u. and $[0, 6.0]$ p.u., respectively.



(a)



(b)

Fig. 7. Modified 39-Bus system: (a) geographical diagram; (b) one-line diagram.

2) *Setup of VIS-RTED and Time-Domain Simulation:* One-hour VIS-RTED ($T = 12$) will be solved on the modified 39-bus system. Assume that the SGs and IBRs have quadratic fuel cost functions and linear reserve cost functions, respectively. The detailed cost data is shown in Table I [39].

To emulate the operation of power systems as realistically as possible, VIS-RTED, AGC, and dynamic load change are integrated into time-domain simulation using CURENT LTB's ANDES [40], [41], which is an open-source Python library for power system analysis and serves as the cornerstone for the LTB [37]. This work provides a representative application of LTB/ANDES, and has been partially documented on the LTB website [42]. The readers can refer to the mentioned resource for comprehensive information regarding the dynamic simulation parameters utilized in this study.

Fig. 8. shows the one-hour load profile with a 1 s time interval for time-domain simulation. The real-time load is synthesized as a forecasted load every 300 s (i.e., every 5 minutes for RTED),

TABLE I
COST DATA

Generator ID	Generation cost		Reserve cost	
	a^{sg}/a^{ibr} (\$/MWh ²)	b^{sg}/b^{ibr} (\$/MWh)	c^{sg}/c^{ibr} (\$)	b_r^{sg}/b_r^{ibr} (\$/MWh)
SG1	0.014	20	500	10
SG2	0.020	20	380	10
SG3	0.019	20	42	10
SG4	0.020	20	380	10
SG5	0.026	20	295	10
SG6	0.021	20	400	10
IBR1	0.001	1	50	20.61
IBR2	0.001	1	50	18.96
IBR3	0.001	1	50	19.15
IBR4	0.001	1	50	20.06

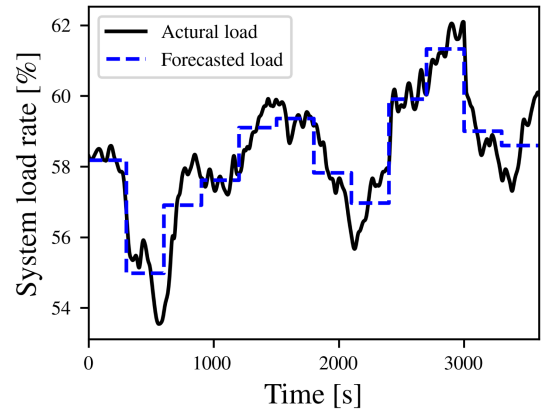


Fig. 8. One-hour load profile.

which is then fed to the VIS-RTED formulated in Section IV. As for the AGC model, the area control error that represents the system imbalance is regulated by a proportional-integral controller followed by a low-order power filter. Then, the area control signal is passed on to individual SGs every 4 s [21].

Because virtual inertia and damping are included in the Jacobian Matrix and fundamentally determine the small signal stability of the dynamics system [43], it is important to verify the stability of the scheduling results before implementation. In each VIS-RTED interval, ANDES verifies the small signal stability of the scheduling results using the 'EIG' function. EIG is an ANDES routine for eigenvalue analysis. Given system parameters (steady state power setting point and dynamic control parameters), it can first calculate the Jacobian Matrix of the autonomous system, and then calculate its eigenvalue. If all the eigenvalues are located on the left half plane, the original system is small signal stable [44], [45]. Otherwise, IBRs' virtual inertia and damping will be fixed to their large default values to guarantee small signal stability and dynamic performance.

C. VIS-RTED Results of IEEE 39-Bus System

This subsection shows the scheduling results and time-domain simulation results of the IEEE 39-bus system.

1) *Scheduling Results:* The total scheduling cost for a one-hour VIS-RTED is \$63,300. Fig. 9 shows the detailed cost results of the 12 scheduling intervals, where (a) is the total

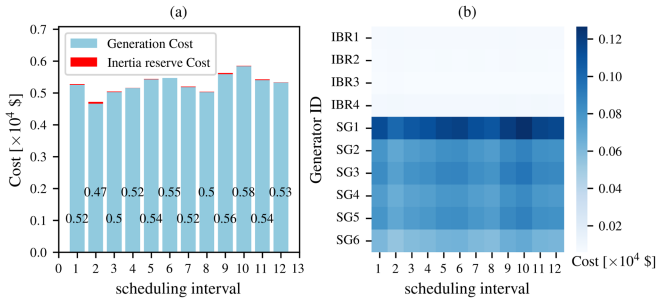


Fig. 9. VIS-RTED cost results: (a) system generation cost and inertia reserve cost; and (b) total cost of each generator.

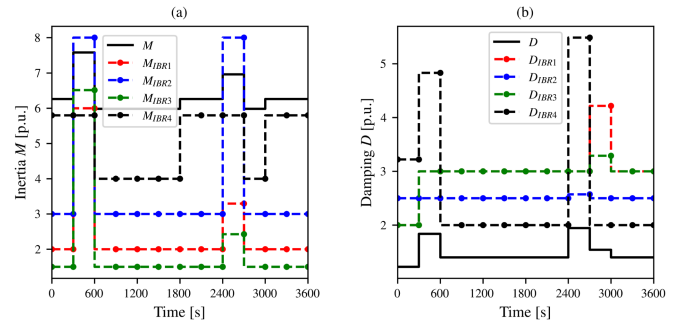


Fig. 11. IBRs inertia and damping: (a) virtual inertia; (b) virtual damping.

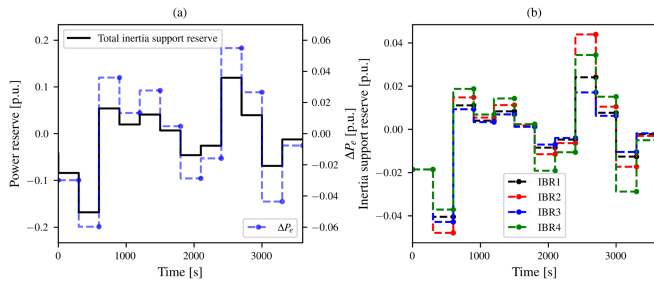


Fig. 10. IBRs inertia support reserve: (a) total reserve along with ΔP_e ; (b) single IBR reserve.

system cost constituted by generation cost and inertia support reserve cost, and (b) is the cost of each SG and IBR in each scheduling interval. In Fig. 9(a), the inertia reserve cost is much smaller than the generation cost (fuel cost). This is because the inertia support reserve of a single interval is around 10% of disturbance ΔP_e . This article assumes the normal load change as a disturbance, which is much smaller than the total generation. If considering large disturbances like generation trips, the cost of inertia support will increase significantly. In addition, because of the low cost of renewable energy, IBRs have a much lower generation cost than SGs in Fig. 9(b).

Fig. 10 displays the inertial support reserve alongside the disturbance magnitude ΔP_e . Notably, the 9th interval exhibits the largest disturbance with $\Delta P_e > 0.04$ p.u., as illustrated by the dashed blue curve in Fig. 10(a). Consequently, the 9th interval necessitates the largest inertia support reserve, as evident from the total inertial reserve depicted in Fig. 10(a) and the individual IBR inertia support reserve presented in Fig. 10(b).

Fig. 11 showcases the scheduling of virtual inertia and damping for each IBR, accompanied by the aggregated M and D parameters of the entire system. Similar to Fig. 10, the 9th interval yields the highest virtual inertia scheduling outcome due to its significant load change. In general, larger values of ΔP_e require greater virtual inertia and, consequently, larger power reserves.

2) *Time-Domain Simulation Results*: Fig. 12 shows the full-order time-domain simulation results in ANDES. The observations are three-fold.

- During the one-hour time-domain simulation, the voltage and frequency in Figs. 12(a)–(b) and 12(e)–(f) are stable,

TABLE II
COMPARISON OF FOUR RTED METHODS

Index	I	II	III	IV
One-hour scheduling cost ($\times 10^4$ \$)	5.73	6.31	6.36	6.33
Inertia support cost ($\times 10^4$ \$)	0	0	0.043	0.014
Inertia support reserve ($\times 10^2$ MW)	0	0	2.58	0.73
Number of IBR capacity violations	0	6	0	0
Number of frequency nadir violations	4	0	0	0
Number of RoCoF violations	0	0	0	0
Single-interval optimization time (s)	0.12	0.13	0.16	0.16

demonstrating the stability of the VIS-RTED scheduling results, particularly the dynamic virtual inertia and damping of IBRs.

- RoCoF constraints are more critical compared with frequency nadir constraints under normal load changes in low inertia power systems. The frequency curves are far from the up and down limits, as shown in Figs. 12(b) and (e), but the RoCoF of the IBRs reaches the limit in Fig. 12(g).
- The scheduled output of IBRs is relatively stable and is higher than SGs due to the low cost of renewable energy resources.

In summary, the one-hour VIS-RTED has been effectively solved and validated on the modified 39-bus system. The proposed strategy enables IBRs to offer secure and cost-effective virtual inertia support to low-inertia power systems, thereby facilitating the integration of a larger number of renewable energy resources.

D. Performance Analysis

To better show the performance of the formulated VIS-RTED in Section III, this article chooses three baselines for comparison, using the same load profile as shown in Fig. 8. Table II shows the comparison results of the following methods. Two critical dynamic curves, i.e., all IBRs' RoCoF, and IBR1's P_e , are plotted in Fig. 13. The detailed setup of the four RTED methods is as follows.

- Method I: ordinary RTED. IBRs work in constant PQ mode [46] with no inertia support capability.
- Method II: ordinary RTED considering dynamic frequency constraints. IBRs work in VSG mode with fixed M and D but don't have inertia support reserves.

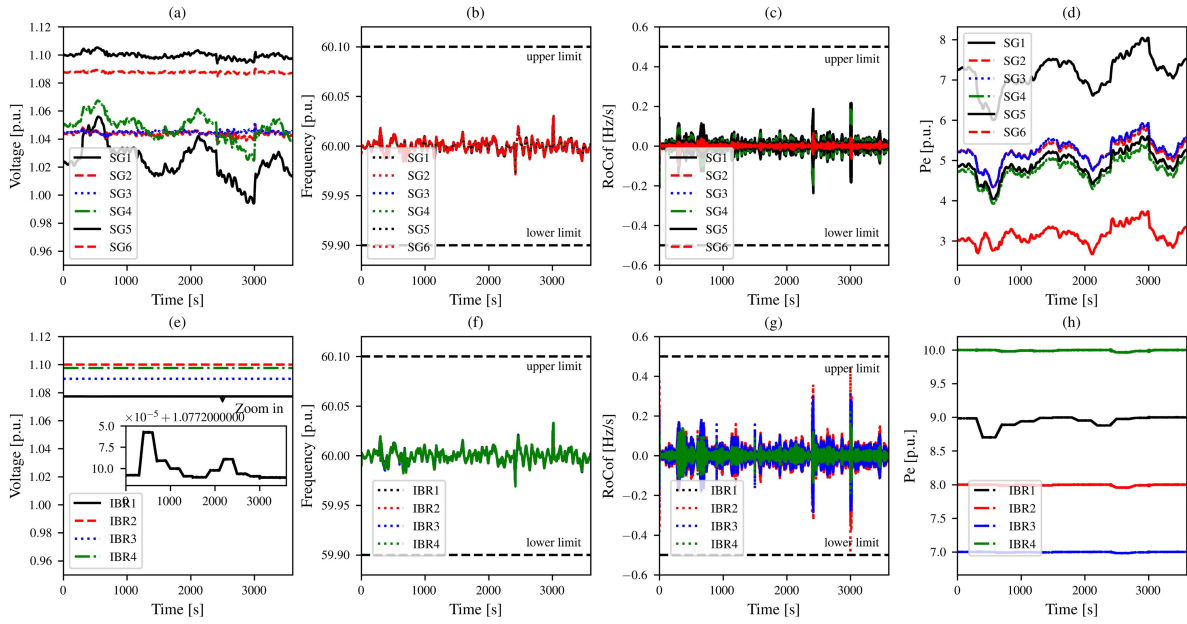


Fig. 12. Dynamics results through full-order time-domain simulation: (a) terminal voltage of SGs; (b) frequency of SGs; (c) RoCoF of SGs; (d) Pe of SGs; (e) terminal voltage of IBRs; (f) frequency of IBRs; (g) RoCoF IBRs; and (h) Pe of IBRs.

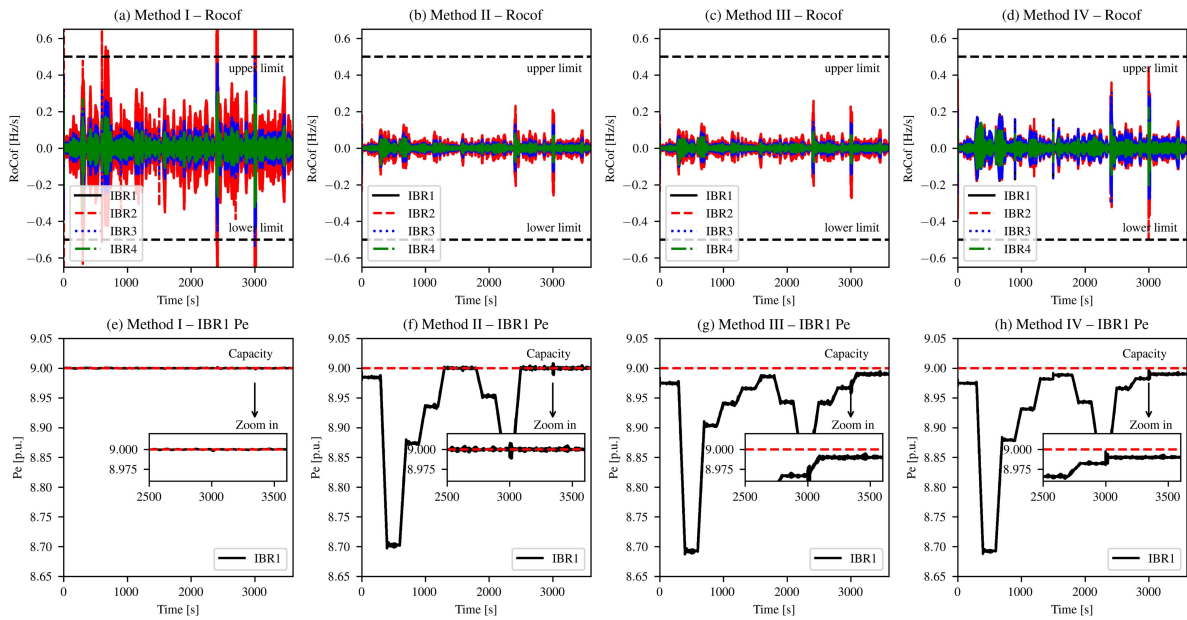


Fig. 13. Comparison of IBRs' RoCoF and IBR1's P_e using different RTED methods: (a) Method I RoCoF; (b) Method II RoCoF; (c) Method III RoCoF; (d) Method IV RoCoF; (e) Method I IBR1 P_e ; (f) Method II IBR1 P_e ; (g) Method III IBR1 P_e ; and (h) Method IV IBR1 P_e .

- Method III: VIS-RTED considering dynamic frequency constraints. IBRs have inertia support reserves but with fixed M and D .
- Method IV: complete VIS-RTED formulation in (25)–(33). As shown in Table II, the four RTED methods are compared from the perspective of scheduling cost, dynamic performance, and computational efficiency, based on which the observations are five-fold.
- Method I, despite having the lowest total scheduling cost, violates RoCoF limits on four occasions due to the inability of PQ-controlled IBRs to provide inertia support to the grid.

- Method II, with its security-constrained formulation, successfully avoids any violations of dynamic frequency constraints. However, during the transient process of inertia support, the output of IBRs exceeds the generation capacity temporarily six times. During the numerical simulation in ANDES, the temporary capacity violation does not result in unfavorable outcomes, primarily because the simulation doesn't include a protection scheme that could limit the output of IBRs providing inertia support or trigger the IBRs to prevent over-current. However, in practical applications, it is common to have additional protection schemes or

control algorithms designed based on the capacity and output of IBRs. Consequently, such violations could have negative effects on the inertia performance of IBRs or even lead to their triggering.

- Method III addresses the issue of IBR capacity violation during inertia support, as observed in Method I and Method II. Nevertheless, it incurs higher inertia support costs and total scheduling costs compared to Method IV. This is because the fixed M_{ibr} and D_{ibr} are determined based on the largest ΔP_e to ensure frequency performance under the worst-case scenario.
- In comparison to Method III, the complete VIS-RTED with decision variables M_{ibr} and D_{ibr} reduces costs while maintaining sufficient inertia support power reserves. This method outperforms the other three baseline methods.
- The computational time for one interval of the economic dispatch model using methods I-IV was very close, as shown by the last row in Table II. This suggests that the integrated dynamic constraints do not impose a significant computational burden using the deep learning assisted linearization method.

The one-hour time-domain simulation results in Fig. 13 further verify the above observations. By examining the RoCoF curves in Figs. 13(a)–(d), it becomes evident that Method I yields the poorest performance due to the absence of inertia support from IBRs. On the other hand, Methods II-IV demonstrate secure RoCoF curves. However, Methods II and III exhibit smaller RoCoF curves compared to Method IV due to the presence of large fixed M_{ibr} and D_{ibr} .

Analyzing the P_e curves of IBR1 in Figs. 13(e)–(f), it is observed that Method I results in a constant IBR1 output without any inertia support. Method II occasionally violates the capacity constraints of IBR1 due to overshoots during the process of inertia support. In contrast, Methods III and IV strictly adhere to the capacity constraints of IBRs while maintaining sufficient inertia support reserves.

In summary, the utilization of the inertia support capability of IBRs enhances the dynamic response of low-inertia power systems. However, ensuring sufficient and secure inertia support requires extra IBR power reserves, which can introduce additional costs. Consequently, an advanced scheduling framework becomes imperative. The proposed VIS-RTED effectively integrates device-level IBR control parameter design into grid-level scheduling, achieving an optimal balance between economy and security. This approach serves as a valuable example of integrating VIS with the existing scheduling framework, offering significant benefits for future low-inertia power systems.

V. CONCLUSION

Although IBRs present low inertia characteristics, their controllability and flexibility allow for the design of an advanced inertia management framework for future low-inertia power systems. Based on this background, this article has proposed the concept of VIS, which targets the security-constrained and economy-oriented inertia management and power dispatch of power systems with large-scale renewable generations. VIS not

only schedules the power dispatch results but also system device control modes and control parameters to provide secure and cost-effective inertia support.

The proposed VIS is integrated into RTED to perform online inertia scheduling every five minutes. VIS-RTED determines the power setting points and reserved capacities of both SGs and IBRs, as well as the virtual inertia and damping of IBRs, to provide sufficient and economic inertia support. Results show that VIS-RTED outperforms the existing RTED strategies in balancing cost-savings and security enhancement. In the future, VIS will be integrated into the other frequency regulated economic dispatch frameworks, such as UC and AGC. Furthermore, the formulated VIS will be enhanced by directly incorporating dynamic performance indices and stability criteria to effectively mitigate security risks.

APPENDIX A

PARAMETERS FOR PLOTTING THE TYPICAL FREQUENCY AND POWER RESPONSE CURVE OF IBRS

Table III shows the parameters for plotting the typical frequency and power curves in Section II-D.

TABLE III
PARAMETERS OF PLOTTING THE TYPICAL FREQUENCY AND POWER RESPONSE CURVE

Item	Value	Item	value	Item	Value
K_g (p.u.)	0.95	R_g (p.u.)	0.05	T_g (s)	6
F_g (p.u.)	0.3	M_g (p.u.)	8	D_g (p.u.)	3
M_{ibr1} (p.u.)	0	M_{ibr2} (p.u.)	1	M_{ibr3} (p.u.)	2
D_{ibr1} (p.u.)	1	D_{ibr2} (p.u.)	1	D_{ibr3} (p.u.)	1
T_{ibr1} (s)	0.3	T_{ibr2} (s)	0.3	T_{ibr3} (s)	0.3

APPENDIX B

PARAMETERS OF TWO-MACHINE SYSTEM

Table IV presents the parameters utilized for solving the single-interval VIS-RTED for the two-machine system and generating the dynamic response curve in Fig. 6.

TABLE IV
PARAMETERS OF TWO-MACHINE SYSTEM

Item	Value	Item	Value
K_g (p.u.)	0.95	R_g (p.u.)	0.05
T_g (s)	6	F_g (p.u.)	0.3
M_g (p.u.)	8	D_g (p.u.)	3
LU_1 (p.u.)	2	LU_2 (p.u.)	2
$P_r^{\max,sg}$ (p.u.)	4	$P_r^{\min,sg}$ (p.u.)	0.1
P_r^{sg} (p.u.)	0.2	f_0 (p.u.)	1
RoCoF _{lim} (Hz/s)	0.5	f_{lim} (p.u.)	0.0017
$P_r^{\max,ibr}$ (p.u.)	1	$P_r^{\min,ibr}$ (p.u.)	0
T_{ibr} (s)	0.3	$M^{\max,ibr}$ (p.u.)	8
$M^{\min,ibr}$ (p.u.)	0	$D^{\max,ibr}$ (p.u.)	6
$D^{\min,ibr}$ (p.u.)	0	D_{ibr} (p.u.)	1
a^{sg} (\$/p.u. ²)	2	b^{sg} (\$/p.u.)	20
c^{sg} (\$)	100	b_r^{sg} (\$/p.u.)	20
a^{ibr} (\$/p.u. ²)	0.2	b^{ibr} (\$/p.u.)	2
c^{ibr} (\$)	10	b_r^{ibr} (\$/p.u.)	2

REFERENCES

- [1] B. She, F. Li, H. Cui, J. Zhang, and R. Bo, "Fusion of microgrid control with model-free reinforcement learning: Review and vision," *IEEE Trans. Smart Grid*, vol. 14, no. 4, pp. 3232–3245, Jul. 2023.
- [2] N. Xue et al., "Dynamic security optimization for N-1 secure operation of Hawai'i Island system with 100% inverter-based resources," *IEEE Trans. Smart Grid*, vol. 13, no. 5, pp. 4009–4021, Sep. 2022.
- [3] L. Fan, "Inter-IBR oscillation modes," *IEEE Trans. Power Syst.*, vol. 37, no. 1, pp. 824–827, Jan. 2022.
- [4] Y. Ryu and H.-W. Lee, "A real-time framework for matching prosumers with minimum risk in the cluster of microgrids," *IEEE Trans. Smart Grid*, vol. 11, no. 4, pp. 2832–2844, Jul. 2020.
- [5] X. Ke, D. Wu, and N. Lu, "A real-time greedy-index dispatching policy for using PEVs to provide frequency regulation service," *IEEE Trans. Smart Grid*, vol. 10, no. 1, pp. 864–877, Jan. 2019.
- [6] B. She et al., "Decentralized and coordinated V-F control for islanded microgrids considering DER inadequacy and demand control," *IEEE Trans. Energy Convers.*, vol. 38, no. 3, pp. 1868–1880, Sep. 2023.
- [7] Y. Deng, Y. Mu, X. Dong, H. Jia, J. Wu, and S. Li, "Hierarchical operation management of electric vehicles for depots with PV on-site generation," *IEEE Trans. Smart Grid*, vol. 13, no. 1, pp. 641–653, Jan. 2022.
- [8] M. Javadi, Y. Gong, and C. Chung, "Frequency stability constrained microgrid scheduling considering seamless islanding," *IEEE Trans. Power Syst.*, vol. 37, no. 1, pp. 306–316, Jan. 2022.
- [9] M. Ghosal et al., "Grid reserve and flexibility planning tool (GRAF-Plan) for assessing resource balancing capability under high renewable penetration," *IEEE Open Access J. Power Energy*, vol. 10, pp. 560–571, 2023.
- [10] M. Qu, T. Ding, W. Wei, Z. Dong, M. Shahidehpour, and S. Xia, "An analytical method for generation unit aggregation in virtual power plants," *IEEE Trans. Smart Grid*, vol. 11, no. 6, pp. 5466–5469, Nov. 2020.
- [11] C. Sun, S. Q. Ali, G. Joos, and F. Bouffard, "Design of hybrid-storage-based virtual synchronous machine with energy recovery control considering energy consumed in inertial and damping support," *IEEE Trans. Power Electron.*, vol. 37, no. 3, pp. 2648–2666, Mar. 2022.
- [12] O. Oboreh-Snapps et al., "Virtual synchronous generator control using twin delayed deep deterministic policy gradient method," *IEEE Trans. Energy Convers.*, early access, Aug. 30, 2023, doi: [10.1109/TEC.2023.3309955](https://doi.org/10.1109/TEC.2023.3309955).
- [13] J. Liu, Y. Miura, H. Bevrani, and T. Ise, "A unified modeling method of virtual synchronous generator for multi-operation-mode analyses," *IEEE Trans. Emerg. Sel. Topics Power Electron.*, vol. 9, no. 2, pp. 2394–2409, Apr. 2021.
- [14] Y. Jiang, R. Pates, and E. Mallada, "Dynamic droop control in low-inertia power systems," *IEEE Trans. Autom. Control*, vol. 66, no. 8, pp. 3518–3533, Aug. 2021.
- [15] U. Markovic, Z. Chu, P. Aristidou, and G. Hug, "LQR-based adaptive virtual synchronous machine for power systems with high inverter penetration," *IEEE Trans. Sustain. Energy*, vol. 10, no. 3, pp. 1501–1512, Jul. 2019.
- [16] Q. Hu et al., "Grid-forming inverter enabled virtual power plants with inertia support capability," *IEEE Trans. Smart Grid*, vol. 13, no. 5, pp. 4134–4143, Sep. 2022.
- [17] Q. Peng, Y. Yang, T. Liu, and F. Blaabjerg, "Coordination of virtual inertia control and frequency damping in PV systems for optimal frequency support," *CPSS Trans. Power Electron. Appl.*, vol. 5, no. 4, pp. 305–316, 2020.
- [18] H. Liu, C. Zhang, X. Peng, and S. Zhang, "Configuration of an energy storage system for primary frequency reserve and inertia response of the power grid," *IEEE Access*, vol. 9, pp. 41965–41975, 2021.
- [19] X. Zhang et al., "A grid-supporting strategy for cascaded H-bridge PV converter using VSG algorithm with modular active power reserve," *IEEE Trans. Ind. Electron.*, vol. 68, no. 1, pp. 186–197, Jan. 2021.
- [20] R. Ofir, U. Markovic, P. Aristidou, and G. Hug, "Droop vs. virtual inertia: Comparison from the perspective of converter operation mode," in *Proc. IEEE Int. Energy Conf.*, 2018, pp. 1–6.
- [21] G. Zhang, J. McCalley, and Q. Wang, "An AGC dynamics-constrained economic dispatch model," *IEEE Trans. Power Syst.*, vol. 34, no. 5, pp. 3931–3940, Sep. 2019.
- [22] Z. Zhang, M. Zhou, Z. Wu, S. Liu, Z. Guo, and G. Li, "A frequency security constrained scheduling approach considering wind farm providing frequency support and reserve," *IEEE Trans. Sustain. Energy*, vol. 13, no. 2, pp. 1086–1100, Apr. 2022.
- [23] P. M. Anderson and M. Mirheydar, "A low-order system frequency response model," *IEEE Trans. Power Syst.*, vol. 5, no. 3, pp. 720–729, Aug. 1990.
- [24] M. Paturet, U. Markovic, S. Delikaraoglou, E. Vrettos, P. Aristidou, and G. Hug, "Stochastic unit commitment in low-inertia grids," *IEEE Trans. Power Syst.*, vol. 35, no. 5, pp. 3448–3458, Sep. 2020.
- [25] Z. Zhang, E. Du, F. Teng, N. Zhang, and C. Kang, "Modeling frequency dynamics in unit commitment with a high share of renewable energy," *IEEE Trans. Power Syst.*, vol. 35, no. 6, pp. 4383–4395, Nov. 2020.
- [26] P. Li, M. Yang, and Q. Wu, "Confidence interval based distributionally robust real-time economic dispatch approach considering wind power accommodation risk," *IEEE Trans. Sustain. Energy*, vol. 12, no. 1, pp. 58–69, Jan. 2021.
- [27] L. Liu, Z. Hu, X. Duan, and N. Pathak, "Data-driven distributionally robust optimization for real-time economic dispatch considering secondary frequency regulation cost," *IEEE Trans. Power Syst.*, vol. 36, no. 5, pp. 4172–4184, Sep. 2021.
- [28] D. Li, Q. Zhu, S. Lin, and X. Bian, "A self-adaptive inertia and damping combination control of VSG to support frequency stability," *IEEE Trans. Energy Convers.*, vol. 32, no. 1, pp. 397–398, Mar. 2017.
- [29] N. Mohammed, M. H. Ravanji, W. Zhou, and B. Bahrani, "Online grid impedance estimation-based adaptive control of virtual synchronous generators considering strong and weak grid conditions," *IEEE Trans. Sustain. Energy*, vol. 14, no. 1, pp. 673–687, Jan. 2023.
- [30] S. Saadatmand, P. Shamsi, and M. Ferdowsi, "Adaptive critic design-based reinforcement learning approach in controlling virtual inertia-based grid-connected inverters," *Int. J. Elect. Power Energy Syst.*, vol. 127, 2021, Art. no. 106657.
- [31] R. Wang, L. Chen, T. Zheng, and S. Mei, "VSG-based adaptive droop control for frequency and active power regulation in the MTDC system," *CSEE J. Power Energy Syst.*, vol. 3, no. 3, pp. 260–268, 2017.
- [32] B. Pawar, E. I. Batzelis, S. Chakrabarti, and B. C. Pal, "Grid-forming control for solar PV systems with power reserves," *IEEE Trans. Sustain. Energy*, vol. 12, no. 4, pp. 1947–1959, Oct. 2021.
- [33] Y. Zhang et al., "Encoding frequency constraints in preventive unit commitment using deep learning with region-of-interest active sampling," *IEEE Trans. Power Syst.*, vol. 37, no. 3, pp. 1942–1955, May 2022.
- [34] Y. Zhang, C. Chen, G. Liu, T. Hong, and F. Qiu, "Approximating trajectory constraints with machine learning—microgrid islanding with frequency constraints," *IEEE Trans. Power Syst.*, vol. 36, no. 2, pp. 1239–1249, Mar. 2021.
- [35] M. Tuo and X. Li, "Security-constrained unit commitment considering locational frequency stability in low-inertia power grids," *IEEE Trans. Power Syst.*, vol. 38, no. 5, pp. 4134–4147, Sep. 2023.
- [36] A. Mehrzad, M. Darmiiani, Y. Mousavi, M. Shafie-Khah, and M. Aghamohammadi, "An efficient rapid method for generators coherency identification in large power systems," *IEEE Open Access J. Power Energy*, vol. 9, pp. 151–160, 2022.
- [37] F. Li, K. Tomsovic, and H. Cui, "A large-scale testbed as a virtual power grid: For closed-loop controls in research and testing," *IEEE Power Energy Mag.*, vol. 18, no. 2, pp. 60–68, Mar./Apr. 2020.
- [38] N. Parsly, J. Wang, N. West, Q. Zhang, H. Cui, and F. Li, "Dime and AGVIS a distributed messaging environment and geographical visualizer for large-scale power system simulation," in *Proc. North Amer. Power Symp.*, 2023, pp. 1–5.
- [39] J. Li, J. Wen, and X. Han, "Low-carbon unit commitment with intensive wind power generation and carbon capture power plant," *J. Modern Power Syst. Clean Energy*, vol. 3, pp. 63–71, 2015.
- [40] H. Cui, F. Li, and K. Tomsovic, "Hybrid symbolic-numeric framework for power system modeling and analysis," *IEEE Trans. Power Syst.*, vol. 36, no. 2, pp. 1373–1384, Mar. 2021.
- [41] H. Cui and F. Li, "ANDES: A python-based cyber-physical power system simulation tool," in *Proc. IEEE North Amer. Power Symp.*, 2018, pp. 1–6.
- [42] B. She, F. Li, and J. Wang, "Showcase of LTB: Virtual inertia scheduling for real-time economic dispatch of IBR-penetrated power systems," 2023. [Online]. Available: <https://ltb.curent.org/showcase/visrted/>
- [43] F. Milano, *Power System Modeling and Scripting*. Berlin, Germany: Springer, 2010.
- [44] S. Chen, Y. Sun, H. Han, S. Fu, S. Luo, and G. Shi, "A modified VSG control scheme with virtual resistance to enhance both small-signal stability and transient synchronization stability," *IEEE Trans. Power Electron.*, vol. 38, no. 5, pp. 6005–6014, May 2023.
- [45] W. Du, Q. Fu, and H. Wang, "Power system small-signal angular stability affected by virtual synchronous generators," *IEEE Trans. Power Syst.*, vol. 34, no. 4, pp. 3209–3219, Jul. 2019.

- [46] B. She et al., "Inverter PQ control with trajectory tracking capability for microgrids based on physics-informed reinforcement learning," *IEEE Trans. Smart Grid*, early access, May 17, 2023, doi: [10.1109/TSG.2023.3277330](https://doi.org/10.1109/TSG.2023.3277330).



AND ENERGY. He is the Student Guest Editor of IET-RPG.

Buxin She (Graduate Student Member, IEEE) received the B.S.E.E. and M.S.E.E. degrees from Tianjin University, Tianjin, China, in 2017 and 2019, respectively. He is currently working toward the Ph.D. degree with the Department of Electrical Engineering and Computer Science, University of Tennessee, Knoxville, TN, USA. His research interests include microgrid operation and control, machine learning in power systems, distribution system plan, and power grid resilience. He was an outstanding reviewer of MPCE and IEEE OPEN ACCESS JOURNAL OF POWER



From 2020 to 2021, he was the Chair of IEEE PES Power System Operation, Planning and Economics (PSOPE) Committee. He has been the Chair of IEEE WG on Machine Learning for Power Systems since 2019 and the Editor-In-Chief of IEEE OPEN ACCESS JOURNAL OF POWER AND ENERGY (*OAJPE*) since 2020. Dr. Li was the recipient of numerous awards and honors including R&D 100 Award in 2020, IEEE PES Technical Committee Prize Paper award in 2019, five best or prize paper awards at international journals, and six best papers/posters at international conferences.

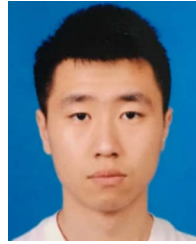
Fangxing Li (Fellow, IEEE) is also known as Fran Li. He received the B.S.E.E. and M.S.E.E. degrees from Southeast University, Nanjing, China, in 1994 and 1997, respectively, and the Ph.D. degree from Virginia Tech, Blacksburg, VA, USA, in 2001. He is the John W. Fisher Professor in electrical engineering and the Campus Director of CURENT with the University of Tennessee, Knoxville, TN, USA. His current research interests include resilience, artificial intelligence in power, demand response, distributed generation and microgrid, and energy markets.



Hantao Cui (Senior Member, IEEE) received the B.S. and M.S. degrees in electrical engineering from Southeast University, Nanjing, China, in 2011 and 2013, and the Ph.D. degree in electrical engineering from the University of Tennessee, Knoxville, TN, USA, in 2018. He is currently an Assistant Professor with the School of Electrical and Computer Engineering, Oklahoma State University, Stillwater, OK, USA. His research interests include power system modeling, simulation, and high-performance computing.



Jinning Wang (Graduate Student Member, IEEE) received the B.S. and M.S. degrees in electrical engineering from the Taiyuan University of Technology, Taiyuan, China, in 2017 and 2020, respectively. He is currently working toward the Ph.D. degree in electrical engineering with The University of Tennessee, Knoxville, TN, USA. His research interests include data mining, power system modeling, and renewable integration.



Qiwei Zhang (Member, IEEE) received the M.S. and Ph.D. degrees in electrical engineering from the University of Tennessee, Knoxville (UTK), Knoxville, TN, USA, in 2018 and 2022, respectively. He is currently a Postdoctoral Researcher with Johns Hopkins University, Baltimore, MD, USA. Prior to this, he was a Research Scientist with UTK. His research interests include renewable integration risk assessment, power system cybersecurity, and electricity market.



Rui Bo (Senior Member, IEEE) received the B.S.E.E. and M.S.E.E. degrees in electric power engineering from Southeast University, Nanjing, China, in 2000 and 2003, respectively, and the Ph.D. degree in electrical engineering from the University of Tennessee, Knoxville, TN, USA, in 2009. He is currently an Associate Professor of the Electrical and Computer Engineering Department, Missouri University of Science and Technology, Rolla, MO, USA, (formerly the University of Missouri-Rolla). He was a Principal Engineer and Project Manager with Midcontinent Independent System Operator (MISO) from 2009 to 2017. His research interests include computation, optimization and economics in power system operation and planning, high performance computing, electricity market simulation, evaluation, and design.